Politecnico di Bari

intestazione repositorydell'ateneo

Exploiting remote imagery in an embayed sandy beach for the validation of a runup model framework

(Article begins on next page)

13 March 2024

Exploiting remote imagery in an embayed sandy beach for the validation of a runup model framework

Nico Valentini[a,b,*], Alessandra Saponieri[b], Alessandro Danisi[b], Luigi Pratola[b], Leonardo Damiani[b]

[a]*BRGM, University of Montpellier, 1039 rue de Pinville, 34000 Montpellier, France*
[b]*Department of Civil, Environmental, Building Engineering and Chemistry (DICATECh), Politecnico di Bari, Bari 70126, Italy*

Abstract

Storm surge and wave runup are key determinants of the potential for beach overwashing during storm events. However, the prediction and quantification of wave runup on embayed beaches is strongly influenced by particular characteristics (e.g., irregular morphology, low tides, absence of swell, etc.) which differ from those on open beaches, and have rarely been investigated in literature. In the present paper, a model framework aimed at predicting wave-induced runup on an embayed sandy beach is validated by means of measurements derived from a video-monitoring station, recently installed in South Italy, during two storm events in 2016. The numerical approach employs MeteOcean forecasted waves within SWAN and SWASH models (in both 2-d and 1-d mode). The combination of multibeam and d-RTK surveys with Unmanned Aerial Vehicle (UAV) imagery provides high resolution depth grid ($0.015\ m$), particularly required in shallow waters, where wave hydrodynamics is highly influenced by the bottom. The results show and discuss the agreement between video measurements and 2-d predictions of runup. A sensitivity analysis of the Manning's roughness factor is needed in 1-d simulations. The accuracy of the empirical formulas in predicting wave runup in an embayed beach is also investigated, showing mainly an overestimation of the observations.

---

*Corresponding author
Email address:* `n.valentini@brgm.fr` (Nico Valentini)

1. Introduction

1.1. Background

The storm surge and wave runup represent the most significant processes in coastal risk assessment models. They greatly influence exposure of coasts to flooding and erosion, recently intensified by climate changes. In swash zone the in-depth knowledge of storm-induced interactions between morphodynamics and hydrodynamics is needed, since sediment transport highly depends on wave up-rush and back-wash, including groundwater behaviour (e.g., Elfrink and Baldock, 2002; Brocchini and Baldock, 2008; Saponieri and Damiani, 2015; Celli et al., 2018). In coastal applications, flooding extent is determined by predicting wave runup, which determines the overwash areas. In such a dynamic coastal environment, despite storm surge can be easily measured from gauge measurements, wave-induced runup estimation is not so feasible. Available approaches for meeting data collection challenges in such a dynamic and energetic coastal environment could be based on the use of remote ground-based observations, numerical modelling and empirical formulas. Numerical models allow to accurately simulate wave propagation from deep-water to swash zone, but they need to be appropriately calibrated under site-specific conditions. In such a context, high-resolution mapping of topography plays a crucial role, since both wave propagation and energy dissipation are strongly influenced by the bottom.

The traditional techniques useful for representing the foreshore Digital Elevation Model (DEM), such as Light Detection and Ranging (LiDAR) and Terrestrial Laser Scanner (TLS), provide wide coverage and good accurate topography. However, they involve high costs, long processing time and are often limited by logistic constraints. The use of Unmmanned Aerial Vehicles (UAVs) represents a new approach to survey relatively large areas in less time and with lower operational costs than standard methods, without affecting the accuracy

2

level in digital land mapping (e.g., Harwin and Lucieer, 2012; Gonçalves and Henriques, 2015; Turner et al., 2016). UAVs make beach recognition more fea-
30 sible for numerical studies, allowing coastal topography to be easily surveyed before and after a storm event with fewer economic and technical limitations. Only few operational constraints still remain, related to environmental conditions (i.e. wind speed) and the difficulty of placing validating artificial Ground Control Points (GCPs) on such irregular areas.

The availability of detailed topography and field data aimed at calibrating numerical models is not always possible. Over the last half century, different field and laboratory studies focused at collecting wave runup data in several conditions, including sandy beaches, structures (e.g., Hunt, 1959; Holman, 1986; Mase, 1989; Nielsen and Hanslow, 1991), as well as gravel beach (Poate et al., 2016) by providing a comprehensive dataset for runup parametrization and a practical predictive tool. However, the large variability of the measurements of this process is remarkable, and evidenced by considerable scatter of predicted results by employing various runup models at single beach, and vice-versa (Atkinson et al., 2017). Most of the empirical formulations relate the wave runup process to deep-water significant wave height, peak period and foreshore beach slope. Hunt (1959) firstly proposed a formulation for the runup, found proportional to the deep-water surf similarity parameter or Iribarren number (Battjes, 1974), as follows:

$$\frac{R}{H_0} = \xi_0 \tag{1}$$

35 where H_0 is the deep water regular wave height, $\xi_0 = tan\beta_f/\sqrt{H_0/L_0}$, $L_0 = gT^2/2\pi$, T the regular wave period and β_f the measured foreshore slope. Holman (1986) made a statistical analysis for the 2% exceedance runup values $(R_{2\%})$ from field data collected on a natural intermediate-to-reflective beach $(tan\beta_f$ from 0.07 to 0.2), by using video images analysis. He found a correlation
40 with the surf similarity parameter, Eq. (2), defined by the significant wave height

3

at an intermediate depth (H_{m_0}) :

$$\frac{R_{2\%}}{H_{m_0}} = \alpha\xi_{0p}^b + c \tag{2}$$

where $a = 0.83$, $b = 1$, and $c = 0.2$. Nielsen and Hanslow (1991) investigated the swash motion on several natural beaches at New South Wales (Australia). By assuming a Rayleigh distribution, the Eqs. (3) and (4) were derived, on the basis of the shape parameter L_{zwm}, Eq. (5):

$$R_{2\%} = 1.98L_{zwm} \tag{3}$$

$$\bar{R} = 0.98L_{zwm} \tag{4}$$

$$L_{zwm} = \begin{cases} 0.05\sqrt{H_{rms}L_0} & \tan\beta_f < 0.1 \\ 0.6\tan\beta_f\sqrt{H_{rms}L_0} & \tan\beta_f \geq 0.1 \end{cases} \tag{5}$$

where H_{rms} is the square root-mean-square height. Ruggiero et al. (2001) created a model in order to examine the predisposition of coastal areas to erosion during extreme events, by using video techniques and aggregating the dataset of Holman (1986). The model accounts for a runup expression, Eq. (6), where β_f represents the slope of the upper-part of the beach, defined in the region between two standard deviations of the water level records from the mean runup elevation:

$$R_{2\%} = 0.27\sqrt{\beta_f H_0 L_0} \tag{6}$$

In the work of Stockdon et al. (2006), based on video runup measurements, in the $R_{2\%}$ formulation, Eq. (7), β_f represents the average slope of a region two

4

standard deviations around the maximum set-up:

$$
R_{2\%} = \begin{cases} 0.043(H_0L_0)^{1/2} & \xi_0 < 0.3 \\ 1.1\left(0.35\beta_f(H_0L_0)^{1/2} + \frac{[H_0L_0(0.563\beta_f^2+0.004)]^{1/2}}{2}\right) & 0.3 < \xi_0 < 1.25 \\ 0.73\beta_f(H_0L_0)^{1/2} & \xi_0 > 1.25 \end{cases}
\tag{7}
$$

Several verification of this formulation are available, among them the analysis of Vousdoukas et al. (2009), which shows an agreement between video-measured
runup at sediment-starved 'pocket' beaches and the recent work of Soldini et al. (2012), which evaluates the influence of seabed on flooding, by using NLSWE and empirical parametrization, providing an expression for the best fit similar to Stockdon et al. (2006).

Recently, two new models for $R_2\%$ has been developed (Atkinson et al., 2017)
from a best fit to the predictions (one forced through the origin and the other with a calculated intercept) from several existing field (Stockdon et al., 2006; Vousdoukas et al., 2012; Ruggiero et al., 2001; Nielsen and Hanslow, 1991; Holman, 1986) and one large-scale laboratory $R_2\%$ data-derived models (Van der Meer and Stam, 1992), for a range of the parameter values used in each model
. The line of best fit forced through the origin is practically identical to Hunt (1959) formula, while the second formulation, Eq. (8), is very similar to Eq. (2).

$$
R_{2\%} = 0.92 \tan\beta\sqrt{H_{m_0}L_p} + 0.16H_{m_0}
\tag{8}
$$

Considering beaches characterized by long wave periods, Mather et al. (2011) highlighted the importance of using not only the foreshore slope, but also the bathymetric profile until the depth of closure, Eq. (9):

$$
R_{max} = CH_0S^{2/3}
\tag{9}
$$

where S acts as a representative nearshore slope and C is a dimensionless coefficient which takes into account the beach morphology. This model is supported with $C = 10$ for open beaches, while required an adjustment of

the coefficient for large embayments where $C = 9$ and small embayments with $C = 6$.

In Mayer and Kriebel (1994), an analytical solution for wave runup over non-uniform beach profiles is discussed, Eq. (10):

$$R = \frac{\beta_f}{2}(X_b - \sqrt{H_o L_o})\left[-1 + \sqrt{1 + \frac{4h_b\sqrt{H_0 L_0}}{\beta_f(X_b - \sqrt{H_0 L_0})^2}}\right] \qquad (10)$$

where the mean runup is derived from a formulation of the average slope between the incipient breakpoint and the runup limit, defined by the Eq. (11):

$$tan\beta_{fb} = \frac{R + h_b}{X_R + X_b} \qquad (11)$$

where h_b is the incipient breaking depth, X_b and X_R are the horizontal distances of the breakpoint from the shoreline and the runup limit, respectively. Douglass (1992) proposed an independent beach slope relationship for evaluating the maximum runup, Eq. (12):

$$\frac{R_{max}}{H_0} = \frac{C}{\sqrt{H_0\ L_0}} \qquad (12)$$

where C is equal to 0.12, calibrated as an empirical coefficient with Holman's data.

Efforts have been particularly directed towards quantifying the influence of beach slope on runup estimation, mainly based on the use of an average beach gradient able to approximate the foreshore slope, greatly influenced by morphological changes during storms (e.g., Ruggiero et al., 2001; Stockdon et al., 2006; Bouvier et al., 2017).

1.2. Objectives and Outline

The present work plans to examine the influence of the beach morphology implementation, at an embayed sandy beach, on wave runup predictions during storm events, characterised by rough hydrodynamic conditions. Methods

6

₉₅ based on both numerical and empirical modelling are implemented. In addition, the aim is to draw up instruments for coastal and maritime management and planning. The study area is presented in Section 2. Measurements from video system and topographic field surveys are used as benchmarks, as described in Section 3 and Section 4. Wave-induced runup is estimated by means of a

₁₀₀ model framework (Section 5), by one-way coupling the spectral 2-d SWAN with the non-hydrostatic 2-d SWASH model, forced offshore with MeteOcean waves forecast data. The nearshore topography derives from a proper combination of Multibeam and d-RTK surveys with a Digital Surface Model reconstructed using UAV imagery (Section 3), providing a high-resolution two-dimensional

₁₀₅ grid. The accuracy of the numerical predictions is then evaluated using the obtained results with measurements derived from the video system and described in Subs. 6.1. Then, the measurements are used to test the empirical formulas in Subs. 6.3. Besides the formulas most used in practice, the models of Mayer and Kriebel (1994) and Mather et al. (2011) are also considered in the present study,

₁₁₀ due to their particular approaches implemented for runup estimation, mainly based on different evaluations of beach slopes and wave parameters. Moreover, the comparison between video measurements and empirical runup calculations allow here to test the validity of formulas in an embayment beach, whose hydrodynamic and morphdynamic behaviours differ from beaches where most of

₁₁₅ parametrization refer to (e.g., Vousdoukas et al., 2009; Soldini et al., 2012). In order to assess the accuracy of runup predictions in 1-d mode, a sensitivity analysis is reported which involved varying the Manning's roughness coefficient, ranging from 0.009 to 0.046 $s/m^{1/3}$, according to the most typical relevant field values for fine-medium sandy beaches (see Subs. 7.1). The main discussions and

₁₂₀ conclusions are highlighted in Sections 7 and 8.

2. Study area

The study area is located in the South of Italy, in the centre of the embayed beach at Torre Lapillo, hamlet of Porto Cesareo (Lecce). The Marine Area of

7

Porto Cesareo is constituted by the typical sub-environment of low-lying coasts,
125 with calcarenitic rocky and sandy beaches. The latter are characterized by a
mean diameter D_{50} equal to $0.47\,mm$ and a D_{95} of $1.38\,mm$. The embayed
beach of Torre Lapillo has an asymmetric planform, characterized by a quite
strongly curved zone to the NW, a gently curved centre and a relative straight
section to the SE (see Figures 1a and 1b).

130 This coastal stretch has been densely urbanized, since the early 1960's, with
remarkable damages to the emerged beach, where the dune was almost totally
dismantled, leading to significant erosion. Moreover, in the period 2007–2009
an increase in the mean sea level (by about $10\,cm$) was estimated (Bruno et al.,
2014; Tsimplis et al., 2013), contributing to shoreline retreat. This was followed
135 by a decrease in 2011, that in 2012 increases slightly again beyond the level of
2009. In particular, the shoreline erosion hot-spots are located in the south-
east, where surveys deployed in 2013-2015 showed an average reduction of the
emerged beach width of about 10 m, with respect to 2009.

The wave climate is moderate to low, with a significant wave height of less
140 than $0.75\,m$ for $44\,\%$ of observations in 2006-2013, compared to $12.17\,\%$ for
$0.75 < H_s < 1.75\,m$ and only $0.66\,\%$ with $H_s \geq 3.0\,m$. The wave heights exceeded
only 5% of the time ($H_{s5\%}$) is around $1.65\,m$ (Petrillo, 2014; Bruno et al., 2019).
The peak period T_p ranging from 3 to $5\,s$ represents the most frequent (about
$31.9\,\%$). Most of the time ($49.7\,\%$) waves approach from the SSE direction,
145 while for $34.8\,\%$ they come from SW. The former is responsible for the rougher
wave conditions. Due to the diurnal microtidal regime along the Ionian Sea, the
tidal range is less than 0.3 m.

In December 2015, a new video coastal monitoring system was deployed and
integrated into the Apulian Region Monitoring Network, managed by the local
150 Basin Authority (AdBP), in order to study both morphodynamic and hydrody-
namic processes (Valentini et al., 2017a,b). It consists of two visible cameras,
framing an area of about $1\,km^2$. A new Shoreline Detection Model (SDM)
for image processing was developed, aimed at extracting shoreline from Timex
oblique images, mainly based on the recognition of sea/sand contours from auto-

8

¹⁵⁵ matic segmented areas. Images are automatically processed and results shared in quasi real-time on a web-portal (http://99.80.236.131/). The SDM was calibrated and tested with successful results (Valentini et al., 2017c), making the system suitable for further investigations such as wave runup monitoring, by extracting from videos the leading edge of the wave up-rush on the beach
¹⁶⁰ face through semi-automated routines, with a minimum of human guidance .

3. Topographical surveys

Both the emerged and submerged beach in the nearshore zone were surveyed by means of different techniques, to obtain a high resolution DEM of the study area. Transect surveys using differential GPS solutions (d-RTK) on the Global
¹⁶⁵ Navigation Satellite System (GNSS) of Apulia region were carried out just before the two storms considered, i.e. on 1st March 2016 and 9th May 2016. Cross-shore beach profiles were surveyed up to a depth of around 0.9–$1\,m$, on 12 and 16 transects, spaced 10 m apart, in the area framed by the two cameras. Dataset quality was evaluated in terms of both horizontal and vertical accuracy,
¹⁷⁰ computed by Leica software Suite (Geosystems, 2001), leading to mean values of $0.0067\,m$ and $0.013\,m$, overall the sampled points, respectively. The nearshore submerged beach was derived from a survey using MultiBeam EchoSounder technology (R2 Sonic 2022), conducted by the management consortium of the Protected Marine Area of Porto Cesareo, under flat wave conditions.

¹⁷⁵ The emerged area framed by one camera ($\approx 10,000\,m^2$) was also surveyed by means of an Aeromax 300 multicopter (Microgeo S.r.l., Florence, Italy). The aircraft was equipped with a Sony α5000 camera, featuring an Exmor™APS HD, 20.1 Mp CMOS sensor. The acquisition at $30\,m$ above the ground level and the camera focal length set equal to $16\,mm$, gave images with a spatial resolution
¹⁸⁰ of $0.44\,cm$.

The UAV imagery was processed by using Structure from Motion (SfM) methodology (e.g., Westoby et al., 2012), which generally proves to be very suitable for environments where a great variability of contrast and prevalent

9

histogram bands occur. Nevertheless, on beaches facing the Ionian Sea, the char-
acteristic features of low vegetated dunes, small-sized ripples and algal blooms
makes UAV surveys challenging.

The SfM algorithm is included in several software packages, coded in differ-
ent forms. The Agisoft Photoscan software (v.1.2.4, build 2399) was chosen for
the analyses, due to its suitability for UAV image post-processing. In the present
study, a mean of 13 overlapping images, taking into account the recommenda-
tions of Fonstad et al. (2013), enabled an accurate topographical reconstruction.
After the image manipulation process (SfM), bundle adjustment was performed
for the dense point cloud reconstruction. The residual errors of the transfor-
mation, computed on the GCPs, resulted in $RMSE$ of $0.017\,m$ in the East,
$0.018\,m$ in the North and $0.011\,m$ in the vertical direction. The overall total
error (3D) was calculated equal to $0.027\,m$, corresponding in the pixel space in
an average value of $0.3\,pixel$ error, with a single outlier of $1.4\,pixel$. A dense
point cloud was produced, by using the *high* quality parameter and *aggressive*
depth filtering option and then interpolated by the Inverse Distance Weight
interpolation method (IDW), to obtain the DEM (Figure 2). The pixel spac-
ing was chosen on the basis of software estimated resolution ($0.0152\,m$), derived
from the averaged distance between points within denser areas. Figure 1a shows
the emerged study area, marked with a black dashed line, the Ground Control
Points (GPCs), the Validation Points (VPs) used for geo-referencing images and
validating the DEM, respectively, and the final DEM.

To assess the vertical accuracy of the UAV-derived DEM, the arithmetic av-
erage and the Root Mean Square of Differences (RMSD) were calculated, based
on the difference between the orthometric heights measured by RTK/GNSS
(VPs) and the elevations derived from the DEM at the same horizontal coor-
dinates. The average difference of $0.033\,m$, is comparable with the absolute
vertical accuracy of the GNSS points ($0.013\,m$) and in good agreement with
previous studies (e.g., Lee et al., 2013; Mancini et al., 2013; Long et al., 2016).
Figure 3a shows the comparison between the elevation of VPs (z_{DGPS}) and
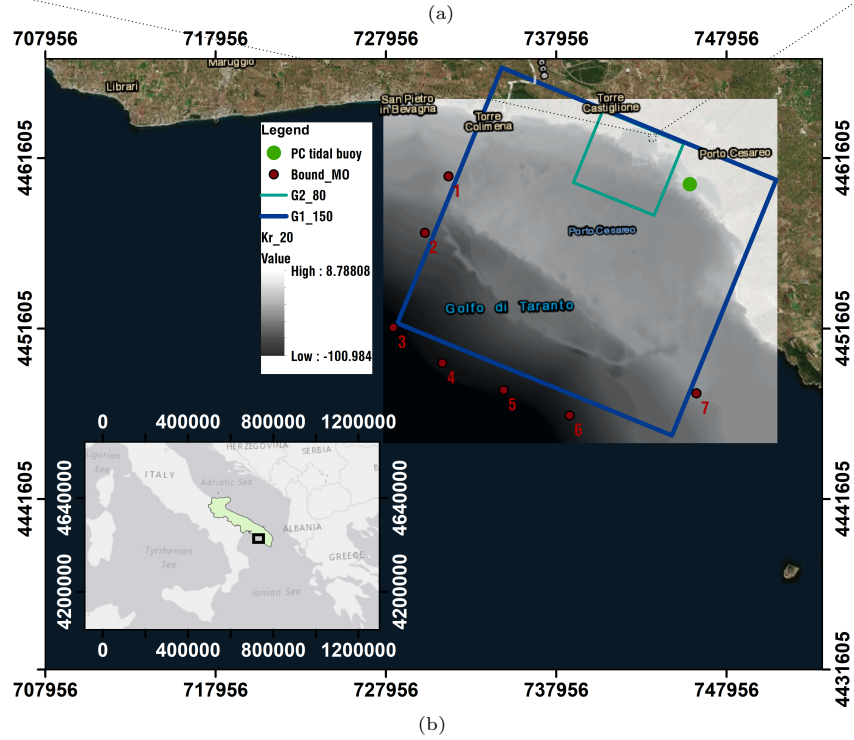the corresponding points extracted from the DEM (z_{UAV}). The regression line
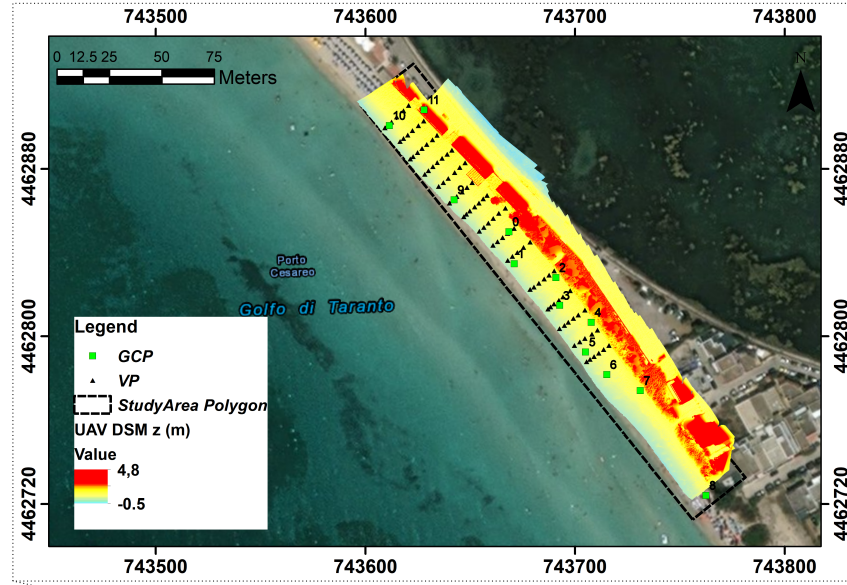
10

Figure 1: (a) DEM obtained from UAV survey. Elevations above sea level measured in m. Highlighted the GCPs location; (b) bottom grid derived from Robust Kriging interpolation with nested grids G_{150} (blue contour) and G_{80} (light green contour); tide gauge (green dot) and MeteOcean boundaries locations (red spots). The inset map highlights the field study area representation. (colour image)
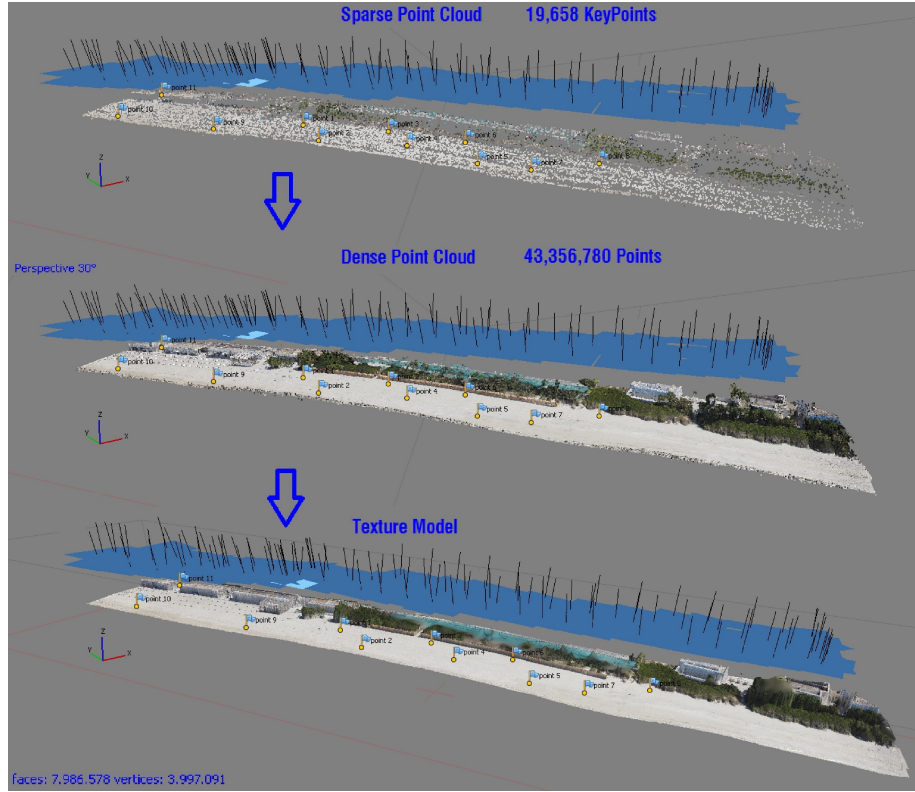
Figure 2: Photogrammetric process at the Torre Lapillo beach; top: creation of sparse point cloud; middle: dense point cloud; bottom: model texture (the reference number on the left bottom of each 3-d sketch defines the KeyPoints and faces/vertices). (colour image)

²¹⁵ shows agreement between measurements, with a fitted line slope close to 1 and R^2 equal to 0.995. In Figure 3b the frequency histogram of the differences $\Delta_z = z_{UAV} - z_{DGPS}$ is reported. The $RMSD$ ($0.044\,m$) is almost equal to the mean value, with a narrow amplitude of the variation, with only one significant outlier, at approximately $0.12\,m$. These validation procedures show average dis-

²²⁰ crepancies at the centimetre order, due to a combination of factors: (i) ground control and validation points were surveyed with d-RTK using reference stations, with their own vertical accuracy ($0.013\,m$); (ii) target points located with care using a plane base under the GPS pole can introduce errors due to movement of the sand; (iii) the interpolation procedure for DEM reconstruction often re-

₂₂₅ sults in artefacts (i.e. ripples of a few centimetres) in a highly-corrugated sandy environment; (iv) the different techniques employed for both surveys are based on remote imagery and intrusive rod acquisitions. Despite these differences, the survey successfully met the requirements for topographic monitoring of common sandy beaches.
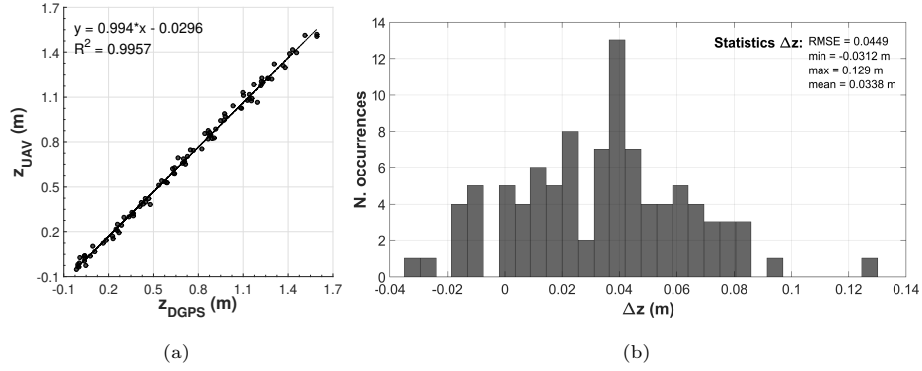

Figure 3: (a) Comparison between the elevation of VPs GNSS data and corresponding points extracted from the UAV DEM. Linear fitting plotted and regression parameters highlighted; (b) frequency histogram for classes of 2 cm and bulk statistic parameters of differences. (b/w image)

₂₃₀ ## 4. Runup measurement from video recordings

Timestack images for wave runup measurements (e.g., Holman and Stanley, 2007; Salmon et al., 2007) were generated in correspondence of two significant storm events, occurred in March and May 2016. Each video had a duration of $30\,min$ with a frame-rate frequency of $5\,Hz$. The image geo-rectification took

₂₃₅ place, after a lens distortion correction, by applying a 3×4 perspective transformation matrix, using homogeneous coordinates (Vousdoukas et al., 2014). The pixel intensities were extracted along the selected cross-shore transects from each frame during video progressions with Python scripting and OpenCV libraries. Timestack pre-processing is crucial before implementing routines for

₂₄₀ swash oscillations recognition, also due to the presence of objects on the beach in the camera's Field of View (FoV) (e.g., geo-textile sand bags, algae, flags,

13

etc.), resulting in dirty or altered images. Moreover, while the wave up-rush on the beach face can be easily identified as a clear feature and easily extracted through semi-automated routines, the backwash phase is less distinguishable,

₂₄₅ do to the saturation of the sand . The edge identification approaches, colour or texture-based, could instead tend to discern the upper envelope of swash motions, particularly for beaches featured by mild to high foreshore slope.

The pre-processing procedure dealt with the masking of the fixed objects visible in the camera FoV, by manually sampling the first frame and applying

₂₅₀ an automatic inpainting of the following ones, before creating the timestack. Furthermore, a combination of filters was applied in the following order: background subtraction (Gaussian Mixture-based); Bi-Exponential Edge-Preserving Smoother (BEEPS, Thévenaz et al. (2012)); variance filter on the grey-coded channel.

₂₅₅ The processing of the timestack edges (wave-by-wave) was then performed using MATLAB-based open-source software, GUI-timestack (https://sourceforge.net/projects/guitimestack/), in order to extract and process the swash time series (Vousdoukas et al., 2012), based on modified Otsu's thresholding method (Otsu, 1979). Final timestack images, re-sampled at $2.5\,Hz$ for easier post-

₂₆₀ processing, had a cross-shore resolution in the range of 2–15 cm, derived from the minimum pixel footprint values along each transect. Figure 4 reports an example of the cross-shore transect location for the calculation of video-derived runup (a) and the relative timestack (b) with the time-variation of the swash leading edge (red line) and the swash extremes.

Cross-shore coordinates of swash extremes were then converted into water-level elevations time series using topographical information derived from the surveys, by assuming negligible morphological changes between video acquisition and d-RTK GPS surveys, performed 2 days before the storm events, often used in practice (e.g. Vousdoukas et al., 2012), if any particular wave event is registered. The estimated elevations represent the total runup, $\eta_{tot}(t)$, defined as follows:

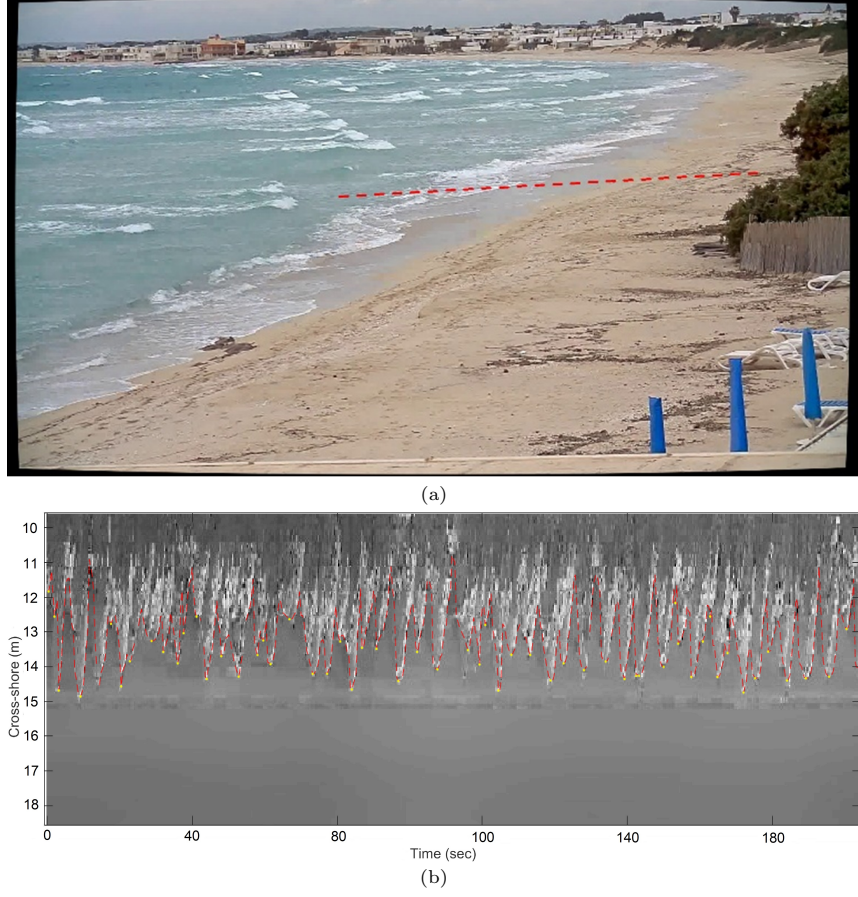$$\eta_{tot}(t) = \eta_{tide}(t) + \eta_{su}(t) + \eta_s(t) + S_{sw}(t) \tag{13}$$

14

Figure 4: (a) Example of cross-shore transect for runup measurement (red dashed line); (b) processed timestack, x-axis and y-axis indicating time and cross-shore distance. (colour image)

where η_{tide} and η_{su} are the tidal and surge heights, respectively, η_s is the maximum wave setup and $S_{sw}(t)$ is the swash-induced water-level fluctuation (Stockdon et al., 2006; Vousdoukas et al., 2009). The wave runup R was derived from the peaks of water level fluctuations $\eta_{wl}(t)$ time series with respect to the still water level (Eq. (14)):

$$\eta_{wl}(t) = \eta_s + S_{sw}(t) \tag{14}$$

265   In the present study, given the relatively small distance between the tide gauge and the study area ($\sim 2\,Km$), tidal and surge heights were assumed to be

15

known since they were directly measured. The runup statistics were calculated for both events, by considering the maximum value of the time series (R_{max} and the 2% exceedance values derived from the cumulative probability density of runup maxima elevations ($R_{2\%}$).

5. The model framework

The numerical approach deals with computing waves approaching the nearshore including the surf zone using the SWAN model (Booij et al., 1996). Initial and boundary conditions were derived from the MeteOcean forecast reanalysis database (Mentaschi et al., 2015), for both storm events considered. The non-hydrostatic SWASH model (Zijlema et al., 2011) was then applied to solve the NSWE until the shoreline for evaluating swash processes. The proposed strategy of one-way nesting MeteOcean forecasted waves into the SWAN model rather than directly into SWASH, allows a good representation of the wave processes to be achieved on meso/fine-scales. The capability of SWAN to produce very accurate shallow water spectral wave conditions, ideal for SWASH implementation, is indeed extensively known and tested. SWASH was chosen since in the literature it is revealed to be numerically more straightforward than similar phase resolving models, in terms of numerical robustness (De Roo et al., 2015), ease of implementation and open source orientation (Celli et al., 2018). Shallow water equations were firstly solved on both 1-d and 2-d domains, for the storm event Ev_2, recorded by camera PC_{vs2} thanks to the availability of the UAV survey, in order to assess the sensitivity of the model to the spatial domain dimension. Then 1-d SWASH simulations were performed for both storm events (Ev_1, Ev_2), to test the influence of roughness coefficient on numerical results.

5.1. SWAN model

SWAN model (version 41.01) set-up includes spectral waves modelling in non-stationary mode, by using two nested regular grids (Table 1). The coarser offshore grid, $16.2\,km$ long and $17.4\,km$ wide, started at a depth of around $90\,m$.

16

²⁹⁵ From a depth of approximately $35\,m$ until the shoreline, wave transformations were analysed on a nested finer regular grid, $4.5\,km$ long and $5.1\,km$ wide (Figure 1b). The bottom grid was derived from a Robust Kriging interpolation of the offshore bathymetry (GEBCO, 2008) and the Multibeam Echosounder survey of the nearshore, with a final resolution of $20\,m$.

Table 1: Computational SWAN grid features (Cartesian coordinates).

GRID	RESOLUTION	x_o	y_o	DIR_x	$m_x * m_y$
G_{150}	$150\ m$	728722.8	4451961.1	$338°$	$115 * 107$
G_{80}	$80\ m$	739010.1	4460207.1	$338°$	$63 * 56$

³⁰⁰ Wave boundary conditions were derived at 7 points from the MeteOcean forecast wave database, resulting from the WaveWatchIII model applied in the Mediterranean Sea. The model, developed and maintained by the DICCA Department of Genoa University (Italy, http://www.dicca.unige.it/meteocean/) is characterized by a high accuracy level in wave forecasting. The dataset in-³⁰⁵ cludes the wind speed and direction as well as the main bulk spectral parameters in terms of significant wave height (H_s), peak period (T_p) and mean wave propagation direction at the peak period (Dir_p). A time step of $30\,min$ was used, with wave boundary condition data included every hour, for a total computational time of $20\,hr$, around the time of observations. Tidal data refer to water ³¹⁰ levels measured at the nearest Porto Cesareo tide gauge.

Figure 5 reports an example of the boundary bulk spectral parameters and the sea levels, at point N. 5 on the SW boundary (Figure 2). In all graphs, vertical dotted red lines indicate the time of runup measurements.

The spectral space was computed at 24 equally spaced propagation direc-³¹⁵ tions $(\Delta\theta = 15°)$ and 24 logarithmically spaced frequencies between $0.04\,Hz$ and $0.6\,Hz$. For the physics, the default parameters are used (breaking constant, JONSWAP formulation of friction, setup, diffraction and triad interactions included, without considering the quadruplet interactions parameter). Wind forcing was not considered, because of the quite small geographic size of
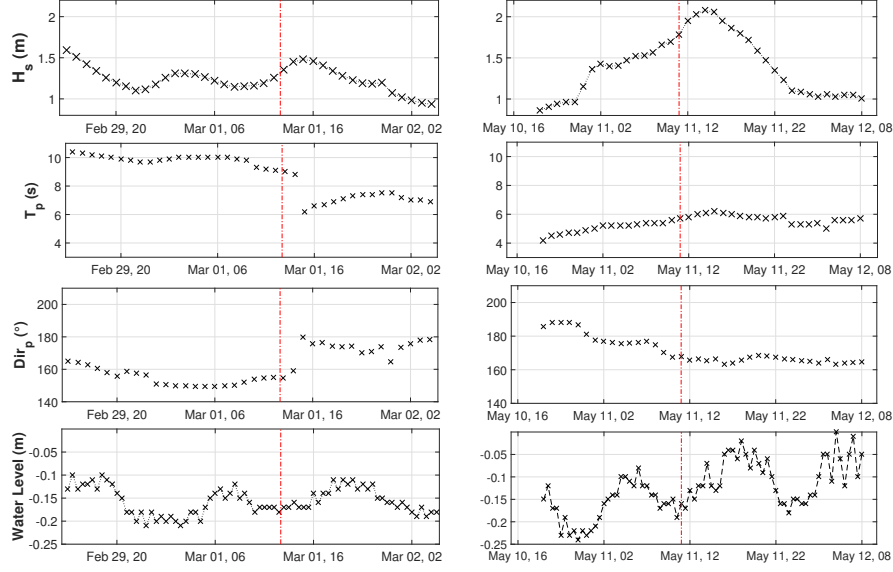
17

Figure 5: Boundary bulk spectral parameters from the MeteOcean model, computed at the point N. 5, and the relative sea level measured by the PC tide gauge for the two storm events. The vertical red dashed lines highlight the time steps under analysis. (colour image)

the computational domain.

5.2. SWASH model

Event Ev_2 was simulated by SWASH in two-dimensional non-hydrostatic mode, over a curvilinear grid (205×1346 grid points). Stationary conditions were assumed (Guimarães et al., 2015). The bottom was generated by merging the Multibeam dataset, with the d-RTK surveyed cross-shore transects and the UAV-derived Digital Surface Model, with a resolution of $0.1\,m$. The computational domain spanned $203\,m$ along-shore and $750\,m$ cross-shore, started from a depth of around $6m$, with a computational grid resolution equal to $1\,m$ and 0.13–$1\ m$, respectively (Figure 6).

Wave spectral conditions were set at each open boundary from the time dependent energy peak derived from SWAN spectral results and the mean water level condition imposed from PC tide gauge measurements. The simulation time
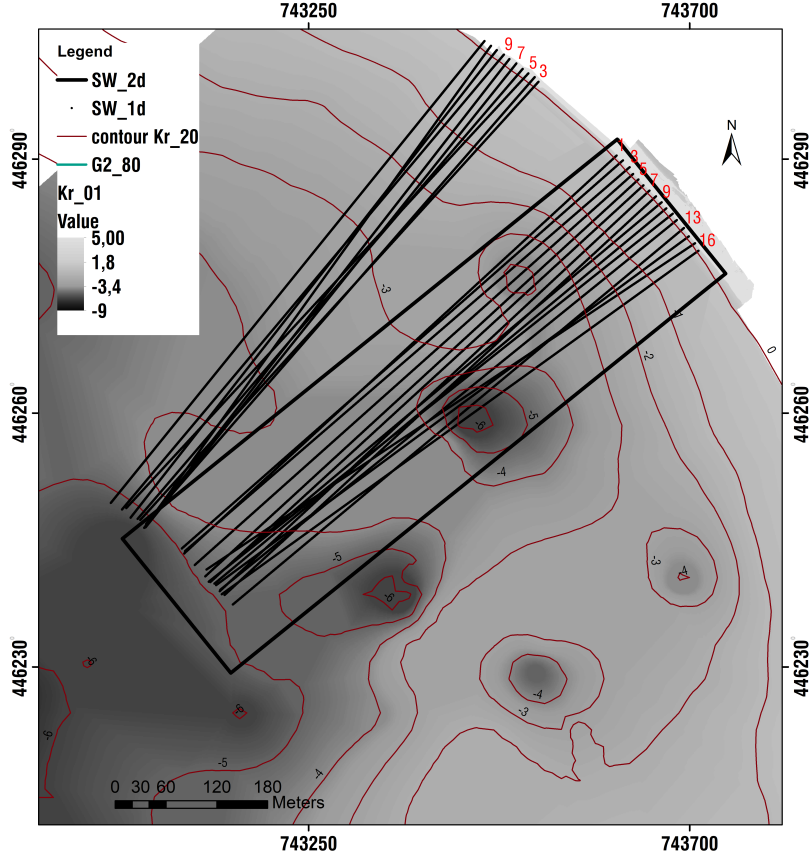
18

Figure 6: SWASH 2-d model boundary (black rectangle) and 1-d transects (black). The contours of the bathymetry Kr_{20} and the raster of Kr_{01} are represented. Transects numbering are in red. (colour image)

was $35\,min$ with a spin-up time of $5\,min$ and a time step of $0.008\,s$. Runup temporal statistics ($R_{2\%}$ and R_{max}) were derived by tracking the wet/dry interface, obtaining the cross-shore temporal variation of water levels at a single longshore location.

Figure 7 shows an example of the spatial variability of SWASH water-level computed after $6\,min$ of simulation and the corresponding timestack. For flooding calculations SWASH considers a time-varying moving shoreline, influenced by the friction coefficient (e.g., Svendsen, 2006; Antuono et al., 2012; Lerma

et al., 2017). In the present work, the Manning's formulation was used for bottom friction with its default value ($c_f = 0.019$).
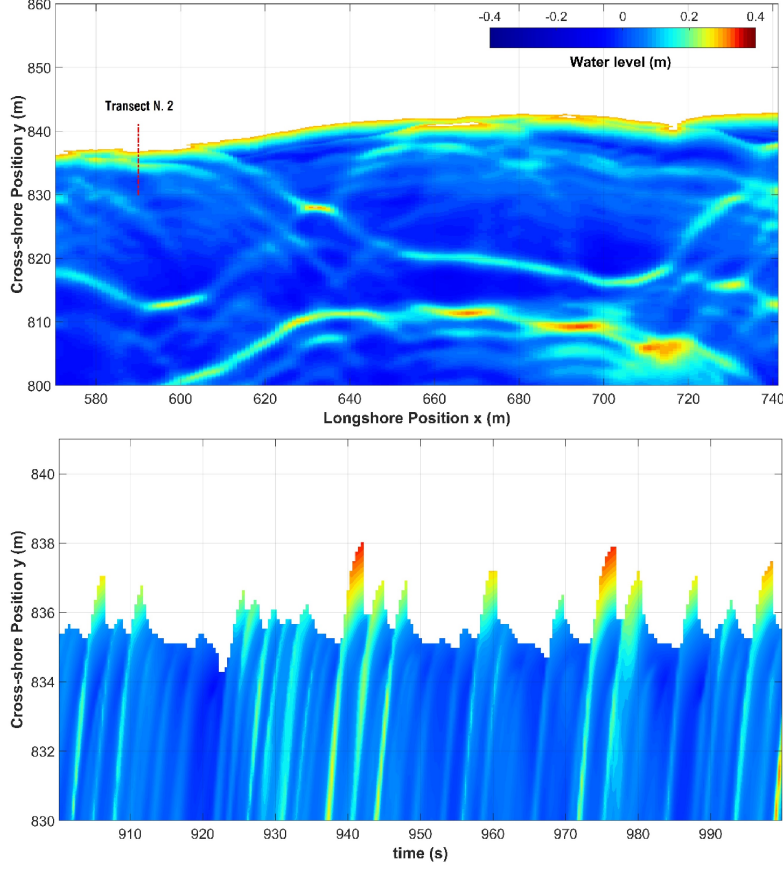

Figure 7: Top: Plan view showing the spatial variability of SWASH water-level computed at 6 min time step (Ev_1); bottom: the timestack shows a portion of temporal cross-shore variation of SWASH water levels at Transect N. 2 (Origin of reference Coordinate system: [x,y]=[7.435838e+05,4.4624715e+06]). (colour image)

In order to investigate 1-d SWASH predictive accuracy, the swash zone hydrodynamics were simulated for the two storm events at 16 cross-shore transects (Figure 6), by assuming along-shore uniformity. Computational 1-d grids were derived from RTK-GPS surveys and nearshore Multibeam bathymetry, with a mean length of $700\,m$ and a grid step of $0.13\,m$ and $0.05\,m$ for transects within

20

the field of view of the first and the second cameras, respectively. The simulation time for each transect test case was set to $35\,min$ with a time step of 0.014 s. The outputs, after a spin-up time of $5\,min$, were requested every $0.4\,s$, consistent with the timestack time discretization. The default minimum and maximum Courant numbers were kept at 0.4 and 0.8, respectively, as in the 2-d case. During each simulation the mean water level condition was imposed by considering the water level measured by the PC tide gauge. Wave spectral conditions were set at the open boundary points of the computational grid domains, derived from the time dependent energy peak of the SWAN spectral results. A simulation of a $5min$ takes approximately 8 hours on 8 cores of a Windows Desktop with an Intel Core i7 5390k, up to 3.2 GHz processor by using mpich2 for parallel MPI implementation.

6. Results

6.1. 1-d and 2-d SWASH modelling

Figure 8 shows the comparison between predicted and measured 2% exceedance and maximum wave runup in correspondence with cross-shore transects where both numerical and video-measurements outputs were valid, in the 2-d as well as the 1-d approach, for the storm event Ev_2. The accuracy of the model is evaluated by the the Root Mean Square Error (RMSE, Eq. (15)), the bias (Eq. (16)) and the percent error, ($Perc\_Err$, Eq. (17)), defined as follows:

$$RMSE(x) = \sqrt{\frac{1}{N}\sum_{i=1}^{n}(x_{i,predicted} - x_{i,measured})^2} \tag{15}$$

$$bias(x) = \frac{1}{N}\sum_{i=1}^{n}(x_{i,predicted} - x_{i,measured}) \tag{16}$$

$$Perc\_Err = \frac{x_{i,predicted} - x_{i,measured}}{x_{i,measured}} \times 100 \tag{17}$$

The comparison of the predicted 2-d values with respect to the corresponding observations shows a mean $Perc\_Err$ of $R_{2\%}$ (R_{max}) equal to $-10.9\,\%$
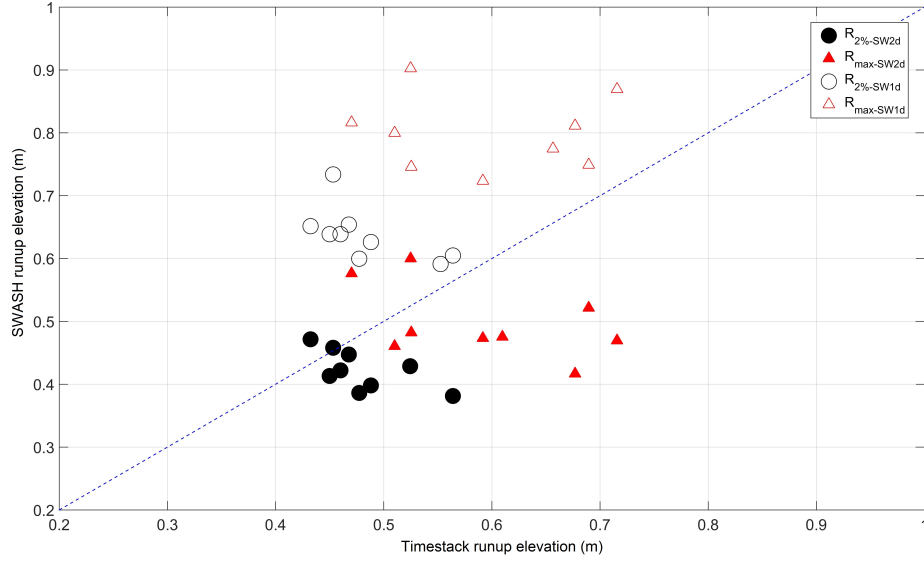
21

Figure 8: Predicted and measured $R_{2\%}$ and R_{max} for both 1-d and 2-d spatial domains over 9 transects, in the area framed by camera PC_{vs2}. (colour image)

370   (-13.3%), a maximum of 32.3% (38.4%) and a minimum of -4.3% (-8.2%). In general, the $R_{2\%}$ shows a better comparison with video-derived measurements with respect to R_{max}, with a RMSE equal $0.084\,m$, against a RMSE equals to 0.156 m, calculated for R_{max}. Moreover, the R_{max} was particularly underestimated for the central cross-shore transects. On the contrary, for the

375   $R_{2\%}$ values, the differences between measured and predicted values are quite the same overall the selected transects. Results mainly show that 2-d numerical results tend to underestimate wave run-up, as confirmed by the negative value of BIAS ($-0.056\,m$). Such a general trend must be partially caused by the vertical accuracy of the UAV-derived DEM, where systematic discrepancies with

380   respect to ground-truth GNSS data are about $0.03\,m$. Conversely, 1-d model predictions tend to overestimates both $R_{2\%}$ and R_{max}. As for 2-d modelling, greater differences are particularly evident for R_{max}.

    In line with previous literature studies (Stockdon et al., 2014) 1-d swash levels are higher than 2-d ones, since the along-shore components of bathymetry,

385   wave groups, and swash oscillations are not fully resolved in 1-d computation.

22

In general, the mean difference for 1-d cases, in terms of $Perc\_Err$, was equal to $30.21\,\%$ for $R_{2\%}$ and $34.1\,\%$ for R_{max}, while the maximum difference of $R_{2\%}$ (R_{max}) was equal to $74\,\%$ ($73.6\,\%$), and the minimum to $25\,\%$ ($0.5\,\%$).

As highlighted before, the transects do not show a spatial uniform behaviour, even if the observed data are not sufficient to uniquely provide an explanation for such dispersion of data. Such effects could not be entirely related to the beach profile modifications during the storm, or accuracy in bottom reconstruction, since the same bottom profile was used in both numerical model and runup calculations from video measurements. The differences could result from the accuracy of the model in simulating dissipation induced by wave breaking and bed friction in both 1-d and 2-d domain. With reference to R_{max}, SWASH predictions are quite the same for all transects, whereas measurements seems to be more affected by the spatial position of transects within the bay. In 1-d simulations the maximum up-rush elevation is mainly related to the nearshore wave propagation and bottom profile at each transect which is almost the same, thus resulting in R_{max} values not affected by the transect position within the bay. In 2-d domain, nevertheless the nearshore dynamics is better reproduced, since both long-shore processes and directional wave energy spreading at the boundary are also considered, the hydrodynamics needs to be calibrated especially in such embayed environment. However, the R_{max} value is not significant enough in the comparison between numerical model and observations, since it can be related to a single swash event. Conversely, the $R_{2\%}$ is more representative of the overall distribution of swash processes. In Figure 8, even a weak negative correlation between predictions and measurements can be observed in both 1-d and 2-d domains. The variance of these differences is actually low. Consequently, even if a large alongshore variability could be deemed as negligible in terms of physical characteristics in the framed area analysed, the monitored transects located in the more straight side of the embayed area show to be better simulated, with respect to the more bordered ones where the runup elevation is underestimated. Moreover, the geo-textiles, placed mostly in the area framed by the cam PC_{vs2}, added some uncertainties in swash computation from the

23

model. Specifically, it has been found the time-stack properly captured the water's edge running up the bump, conversely for the model, where in few cases it appeared to be stuck.

6.2. The influence of the Manning's friction

A sensitivity analysis of the SWASH model capability in predicting nearshore hydrodynamics was performed by varying the Manning's roughness factor from 0.009 to 0.046 $s/m^{1/3}$, according to the most typical relevant field values (Benson and Dalrymple, 1967). Figures 9 and 10 show the predicted and measured $R_{2\%}$ and R_{max}, respectively, nondimensionalized by the offshore significant wave height, for different values of bottom friction coefficient (a), with the relative bias and $RMSE$ (b) over all the selected transects.

Specifically, the values $n = 0.043\,s/m^{1/3}$ and $n = 0.04\,s/m^{1/3}$ reveal the best fit in predicting the timestack measurements, with respect to $R_{2\%}$ calculation and to R_{max}, respectively. For the first variable the $RMSE \cong 0.05\,m$ and the $bias \cong 0.018\,m$, while for R_{max}, $RMSE \cong 0.075\,m$, and $bias \cong 0.01\,m$. The 1-d simulation results aimed at runup prediction are satisfying only with an ad-hoc calibration of the friction coefficient, differently to the 2-d simulation, where the model achieves optimal performance by using the default value. In fact, the infragravity component of the overall spectral wave energy has been previously reported to be often overestimated by the SWASH model (1-d), particularly in the surf zone (Zijlema et al., 2011; Conde-Frias et al., 2017). This overestimation mainly depends on the standing-wave component caused by reflection of infragravity waves close to the shoreline (Zijlema and Stelling, 2008), together with errors associated with the bottom friction estimate, which acts as a primary mechanism by which the longer waves lose energy (Smit et al., 2014), and finally on the not fully solved alongshore components of the hydrodynamic processes, which affect dissipation processes in the swash zone.

6.3. Empirical runup

This subsection contains the results of the empirical runup formulations for the storms considered, when reliable corresponding measurements were avail-
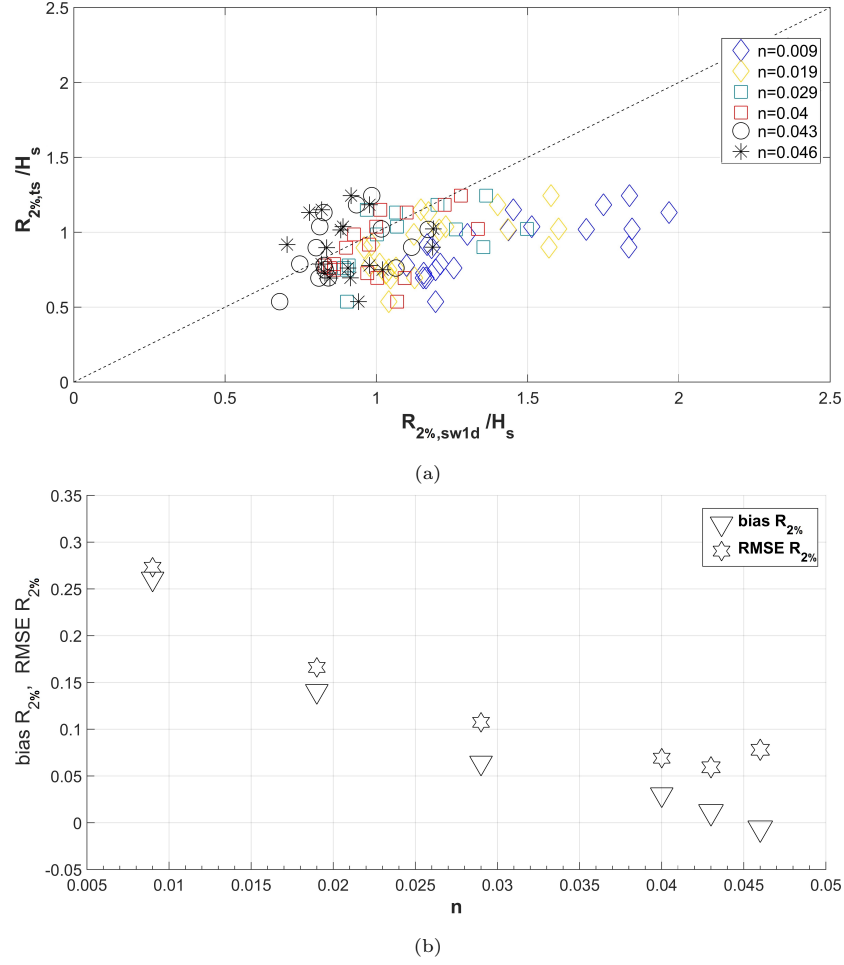
24

Figure 9: (a) Predicted and measured $R_{2\%}$ for transects analysed, both quantities are normalized to the significant wave height at relative boundary; (b) sensitivity of computed $R_{2\%}$ to bottom friction coefficients ('n'). (colour image)

able. A total of 8 models, well described in literature (Atkinson et al., 2017; Vousdoukas et al., 2012) are tested and discussed. The models used have been found to be the most accurate for the data sets upon which they were built (Atkinson et al., 2017) and they can be considered the most useful in practice for most applications in coastal engineering. Among them, the model from Mather et al. (2011) highlighted the importance of using not only the foreshore
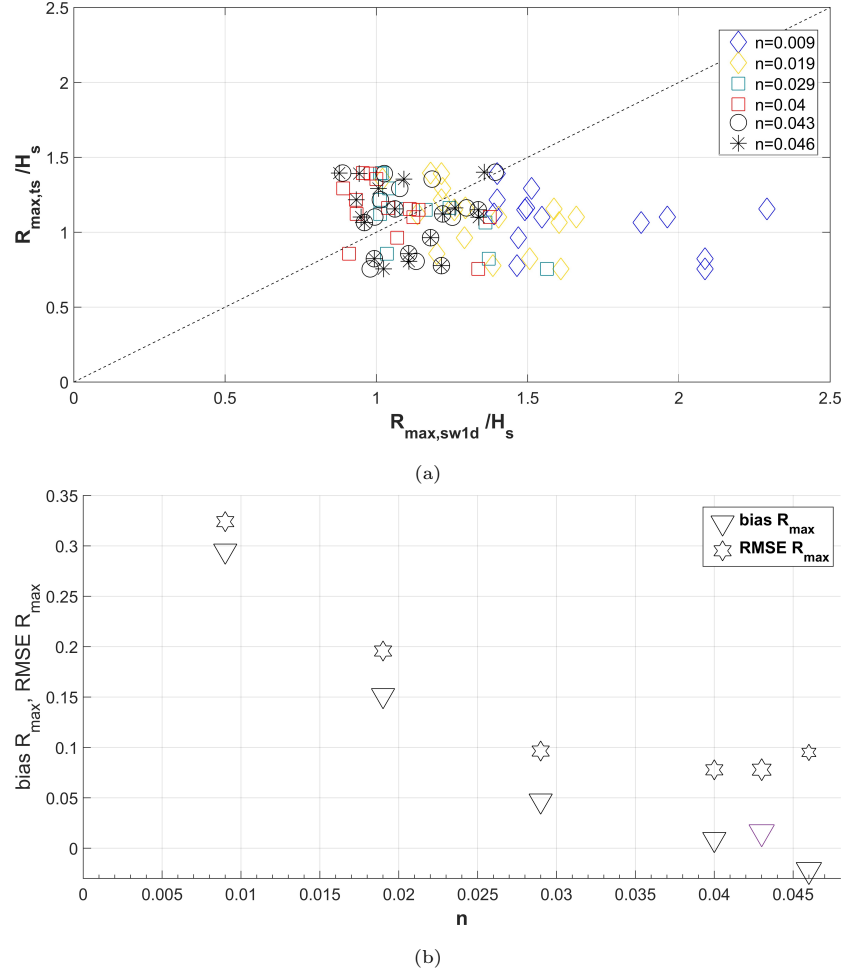
450

25

(a)

(b)

Figure 10: (a) Predicted against measured R_{max} for transects analysed, both quantities are normalized to the significant wave height at relative boundary; (b) sensitivity of computed R_{max} to bottom friction coefficients ('n'). (colour image)

slope, but also the bathymetric profile until the closure depth, (Eq. (9)):

Table 2 summarizes the mean values of $R_{2\%}$ and R_{max} over the reliable transects analysed (n.16), representative of the gently curved centre of the large embayed beach of Porto Cesareo. Both quantities refer to the offshore spectral wave parameters (e.g., H_s, L_{0p}, T_p), derived from averaging the MeteOcean model inputs on points N. 4, 5, 6 and 7 in Figure 1b located at the SW boundary

455

26

of SWAN grid G_{150}.

⁴⁶⁰ Typically, when measurements at shallow or intermediate depth are available, a reverse shoaling to deep water using linear wave theory is suggested (Stockdon et al., 2006). By using the results from SWAN model prior to breakpoint, the wavenumber is calculated from the dispersion relationship, the shoaling coefficient K_s is calculated according to Nielsen (2009), deepwater wave height ⁴⁶⁵ Ho is determined as $H_o = H_b/K_s$.

Table 2: Summary of the runup predictions derived from empirical formulations, as mean values over n.16 transects, for the two storm events Ev_1 and Ev_2 investigated. Between brackets the values computed using the equivalent significant wave height.

	Ev_1	Ev_2	$MeanErrorPerc.$
$R_{2\%}(m)$			
Timestack	0.49	0.48	-
Holman (1986)	0.92 (0.82)	1.13 (0.95)	109 (82) %
Nielsen & Hanslow (1991)	0.88 (0.76)	0.8 (0.72)	72 (52)%
Mayer & Kriebel (1994)	0.52 (0.44)	0.56 (0.49)	10 (-4) %
Ruggiero et al. (2001)	0.93 (0.78)	0.79 (0.66)	76 (48) %
Stockdon et al. (2006)	0.97 (0.79)	0.88 (0.76)	89 (59) %
Atkinson et al. (2017)	0.94 (0.83)	0.85 (0.74)	83 (61) %
$R_{max}(m)$			
Timestack	0.6	0.59	-
Douglas (1992)	1.23 (0.95)	1.17 (0.87)	102 (53) %
Mather et al. (2010)	0.57 (0.52)	0.69 (0.60)	6 (-5) %

Most of the models investigated partly overestimate the observed wave runup, both $R_{2\%}$ and $R_{max\%}$, with a mean percentage error of more than 70 %. As also suggested in Stockdon et al. (2006), this bears witness to the fact that runup prediction using deep water buoy measurements may result in signif- ⁴⁷⁰ icantly higher results than those obtained using a wave height measured at a local buoy (closer to the shore), where nearshore wave processes can be properly

taken into account. Accordingly, by reverse shoaling intermediate depth wave height to deep water, by applying the linear wave theory, the mean percentage error, for the majority of the models, decreases at around the 50 to 60%. The

475 models showing the best performance at this embayed system are from Mayer and Kriebel (1994) and Mather et al. (2011), which both of them, differently, take into account the entire surf area for the computation of the peaks in swash oscillations.

7. Discussion

480 *7.1. 1-d and 2-d SWASH modelling*

The differences in runup for the two dimensional spaces can be explained by several physical/numerical factors. In order to retrieve reasonable causes for this behaviour some concepts need to be highlighted. It must be noted that the same radiation boundary condition was imposed within the investigated

485 area to simulate entering waves without reflections. The significant wave height modelled in 1-d (red line) and 2-d (blue line) domains are reported in Figure 11, for a representative transect (n.9). Moreover, the wave power spectral density at the representative boundary, breaking and surf representative sections are reported.

490 The two implementations do not show any substantial difference until the breaking zone, even if the 2-d signal shows higher oscillations which increase approaching the breaking zone. Within the surf zone, greater attenuation is highlighted for the 2-d model, with respect to the 1-d, with consequent differences in runup calculations, due to discrepancies in wave energy propagation

495 modelling.

The SWASH breaking mechanism, here applied, is based on Hydrostatic Front Approximation (HFA) algorithm (Smit et al., 2014), automatically activated when a low number of layers is implemented in the model. The HFA approach is used in both spatial domains. In both domains, before incipient

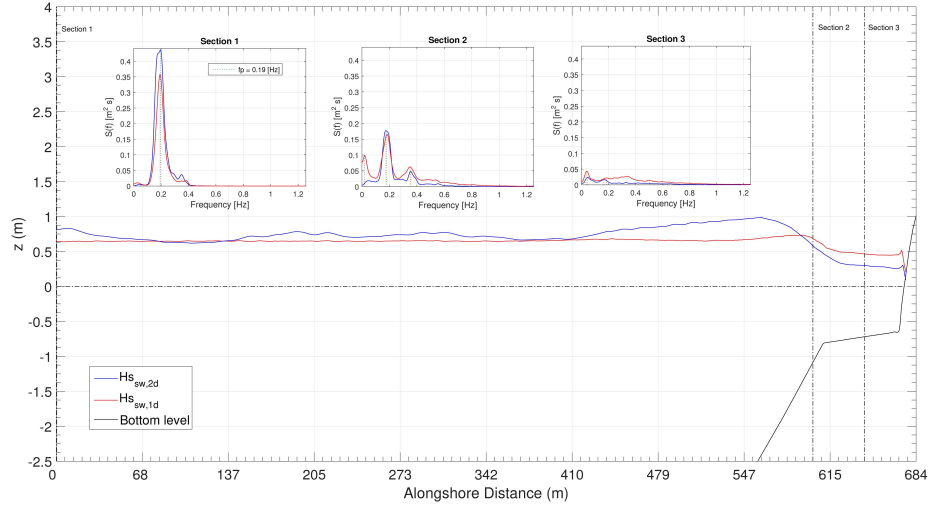500 wave breaking, an increase in wave energy occurs. In 2-d domain the energy

28

Figure 11: Cross-shore variability of H_s between SWASH 1-d and 2-d and spectral transformation of water levels output comparison for the two spatial domains, at three representative sections (Transect N.9). (colour image)

is mostly concentrated at the peak frequency, wave directionality tends to reduce the forcing waves in the infragravity frequencies (Herbers et al., 1994). In the 1-d model, instead, the spectrum shows wave energy components at low-frequencies and a reduction of the energy at the peak frequency. In the surf ₅₀₅ zone, 2-d model spectra mainly highlight the breaking-induced dissipation. In the 1-d spectra infragravity waves are assumed to dissipate by transferring their energy back to higher frequencies, by infragravity-wave breaking (Henderson et al., 2006) and by bottom friction (secondary importance). The higher wave energy content simulated in 2-d induces a seaward shift of the first breaking ₅₁₀ section, with respect to the 1-d domain, with a consequent broadening of the surf zone.

According to Rijnsdorp et al. (2014), SWASH has a tendency of overprediction of the outgoing components of infragravity waves, furthermore Rijnsdorp et al. (2015) highlighted a behaviour with frequency dependency hence, ₅₁₅ a near-zero reflection for high frequency infragravity waves, the inverse for low frequency components. For this reason, explorative analysis using cross spectral

29

analysis via magnitude-square coherence of runup and surf zone water levels was conducted. A standing-wave component in the infragravity frequencies can be observed in 1-d runs with respect to the 2-d domain. A kind of nodal structure

₅₂₀ in the cross-shore variation of these low frequency components of the bulk significant wave height, which tends to increase shoreward, further highlighted the occurrence of such phenomenon. This factor most probably led to such results and is associated with the different highlighted simulated contributions of alongshore dissipation mechanisms of swash via non-linear and frictional processes.

By comparing both the 1-d and 2-d numerical models with the runup measurement derived from video analysis, the results show that the 1-d model systematically overpredicts the timestack results. The influence of the seabed friction, for NLSW equation models, in wave runup prediction and overtopping due to a global damping of the flow, is well-known (e.g., Tuan and Oumeraci, 2010; Suzuki et al., 2011; Antuono et al., 2012). Different formulations are implemented in SWASH for the dimensionless friction coefficient calculation c_f. In the present study, the formula based on Manning's roughness coefficient n is used, Eq. (18):

$$c_f = \frac{n^2 g}{h^{1/3}} \tag{18}$$

₅₂₅ The default value for this parameter in SWASH was set to $0.019 \, s/m^{1/3}$. Currently, there are not unequivocal results or suggestions available in the literature about its optimal variability. Among several parameters under coastal regime, n mainly varies with grain diameter (e.g., Reis and Gama, 2010). For instance, previous studies (e.g., Suzuki et al., 2011) suggest that the behaviour

₅₃₀ of smooth materials in the laboratory could be well represented by using a value of approximately $0.01 \, s/m^{1/3}$, while a Manning's coefficient equal to about $0.02 \, s/m^{1/3}$ is suggested for sandy materials with a diameter close to $1 \, mm$, as in the present field case. Due to such a range of variability of the coefficient and the difficulties between field and laboratory measurements, it represents a

₅₃₅ useful and straightforward parameter for numerical model calibration.

Figure 12 shows an example of the spatial variation of significant wave height

30

derived from the zero-order moment of the spectrum (H_{m0}, Figure 12a) and wave setup (η_s, Figure 12b) for transect N. 6, modelled by SWASH in a 1-d spatial domain, with different bottom friction values. Seaward from the first breaking point, neither quantity is very sensitive to bottom friction. This be-

540 haviour was observed for all sections analysed. On the contrary, within the surf zone area, both significant wave height and setup become more sensitive to n because of the increasing bottom effects on propagating waves. No influence of the friction factor on the wave peak period was observed.

545 One source of error in SWASH predictions is due to the changes in beach morphology, which are not straightforward to estimate, since submerged and emerged beach were surveyed in different periods. Geoprocessing surveys show that in the zone straddling both GPS and Multibeam, at approximately $1\,m$ depth, the gap over the whole investigated area was less than $5\,cm$. The DEM

550 is, indeed, obtained by neglecting any substantial modification of the submerged morphology. However the seasonal and interannual variability of hydrodynamics may change short-term morphodynamics, by introducing errors in the wave runup propagation and calculation. Despite such limitations, which are very common in practice, the model shows acceptable responses for the events con-

555 sidered, with respect to the video observations.

The implementation of such model framework aimed at calculation of potential for overwashing of beaches during storm events is feasible for being included as a warning system. Bed level measurements are logistically consuming, methods spans from video-based stereometric measures (Holland and Puleo, 2001), ultra-

560 sonic and resistivity sensors are available. Most of them could be used for the analysis of the intertidal area only, which is not beneficial on microtidal coastal area. In order to address this typical shortcoming, particularly during storms, it would be beneficial to implement an instrumentation frame capable of recording the wave-by-wave bed level changes. This would lead to the possibility of val-

565 idating a numeric solution for describing the morphodynamic behaviour of the embayed system that could to be included, later on, in the model framework. Considered the computational cost of SWASH simulations, an operational fore-
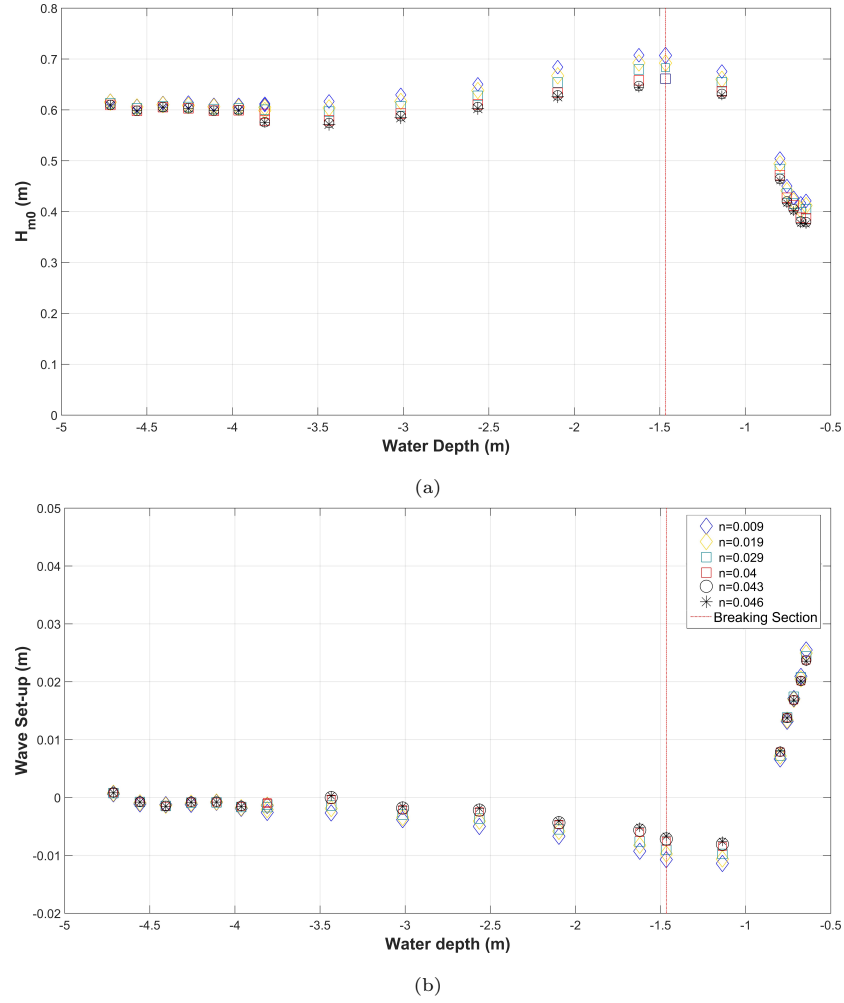
31

(a)

(b)

Figure 12: Sensitivity of significant wave height H_{m0} (a) and wave setup η_s (b) for varying Manning's coefficient. (colour image)

casting system could be built by choosing opportunely defined thresholds on the forecasting offshore wave conditions.

570 *7.2. Insights on runup formula*

Runup studies, upon which most of available empirical parametrisations have been based, have been mainly carried out on open sandy beaches, approached by oceanic swell, extreme storm waves and tide waves even if the formulations are

32

often used in several different morphologies and broad wave climate conditions,

⁵⁷⁵ providing a wide scatter of results. Few runup studies have been performed on such embayments (Vousdoukas et al., 2009). Predictive models of wave runup, and specifically those investigated in the present work, traditionally focus on the beach foreshore slope β_f as the key determinant of $R_{2\%}$, under both regular (Hunt, 1959; Mase, 1989) and irregular waves (Holman, 1986; Nielsen and

⁵⁸⁰ Hanslow, 1991; Ruggiero et al., 2001; Stockdon et al., 2006). Whereas, Douglass (1992) argued that the maximum runup is not influenced by the beach-face slope, the model of Nielsen and Hanslow (1991) assumes no dependence on beach slope only for $tan\beta_f \leq 0.1$, as is the case for the majority of the analysed transects, with two exceptions. As observed during laboratory experiments described in

⁵⁸⁵ Blenkinsopp et al. (2016), empirical formulas better predict wave-induced runup under controlled boundary conditions since waves are perpendicular to the shore and not affected by wave direction. At field sites, inversely by properly account for the propagation processes and reverse shoaling the measurements at shallow or intermediate depths, the resulting equivalent deep-water values lead to

⁵⁹⁰ a more reasonable accuracy (Subs. 6.3). Moreover, the inundation process on a tideless embayed beach has been demonstrated to be better captured by using the breaking wave height (Sancho et al., 2012). On the other hand, as highlighted in Stockdon et al. (2014), such parametrisations generally suffer from systematic errors, due to site-specific characteristics that are not included in

⁵⁹⁵ the models. The exception are empirical models whose different and well-fitted performance is largely explained by the approaches used for the calculation.

As the time of writing, the $R_{2\%}$ evaluated by the analytical solution of Mayer and Kriebel (1994) best agrees with the video measurements for both events, most probably due to the use of the so-called *effective slope* in the runup cal-

⁶⁰⁰ culation. The *effective slope* derives from Saville's method (Thorndike Saville, 1957) which introduces, over arbitrary geometries, an appropriate average slope for predicting runup on a composite-slope, and allows the entire active surf zone to be taken into account, between the wave break point and the runup limit, Eq. (11). The $R_{2\%}$, Eq. (10), is then calculated with reference to the distance

33

$X_b(t)$ and the corresponding time series of $h_b(t)$ are taken from 2-d SWASH simulations. However, this makes this formulation not perfectly adapted for an easy, direct use, since it also uses information derived in this case from numerical modelling results.

The formulation which best predicts the R_{max} is that of Mather et al. (2011), who correlates the maximum wave runup height with the shape of the offshore profile as well as the foreshore slope and this combination plays a crucial role for such morphological system. Such an offshore limit is defined until a specified point on the sea bed at a certain distance x_h and depth h seaward of the surf zone, according to the following relationship:

$$\frac{R_{max}}{H_0} = \left(\frac{x_h}{h}\right)^p \tag{19}$$

where p is comparable with the coefficient of power law in Bruun's equilibrium profile (Bruun, 1954). The dimensionless coefficient C of Eq. (9) applied in this work is assumed equal to $= 9$ (large embayment condition), while S is referred to a representative nearshore slope, calculated until the closure depth, estimated from the formula from (Birkemeier, 1985), at a depth of $5.4\,m$.

8. Conclusions

The capability of predicting wave-induced runup on an embayed sandy beach by using different approaches has been evaluated in the present work. Video observations are compared with numerical results derived from one-way coupling of opportunely nested SWAN and SWASH models, forced by the MeteOcean forecast wave data. A non-standard photogrammetric technique demonstrated the potential of UAV imagery for deriving a high-resolution, accurate and reliable topographical input, which is particularly useful for fragile and complex coastal areas. The comparison between 2-d runup predictions and video observations demonstrates an overall good representation of swash zone hydrodynamics, based on the data of the storms available. The percentage error in $R_{2\%}$ calculation is equal to around 10%, with a RMSE of $0.084\,m$. Higher swash levels in

34

1-d SWASH runs lead to overestimating the video measurements. The model runs, by using the two spatial domains, simulated differently the nearshore processes with spectral components that particularly at infragravity frequencies
₆₃₅ contributes dissimilarly to the total energy. A major decrease in water level amplitudes in the swash zone for the 2d runs can also be ascribed to better suited alongshore dissipation mechanisms of swash via non-linear and frictional processes, with respect to 1d. Since constrained model-parameter assumptions in the default configuration often lead to drawbacks in numerical models results,
₆₄₀ for the present work a sensitivity analysis of the Manning's friction coefficient on swash prediction, was conducted in the 1-d spatial domain. Results suggest that when the SWASH model is used for estimating real-world hazards, users should think carefully about choosing an appropriate roughness, by conducting sensitivity analysis and calibrating the model.

₆₄₅ The reliability of the empirical formulations has been investigated, by comparing modelled with measured results. This study, although characterized by a database at single field site, emphasized that the empirical models forced by raw deepwater wave conditions overestimate the video-measurements by more than 70%, as well as numerical predictions. By reverse-shoaling the simulated
₆₅₀ significant wave height (deep-water equivalent wave height) at shallow depth, so by partly including the complex hydrodynamic processes occurring during wave propagation, the mean percentage error is reduced at 50 to 60%. The high influence of both nearshore and surf zone slopes is taken into account in the models of Mayer and Kriebel (1994) and Mather et al. (2011), which are
₆₅₅ capable of better capturing the runup phenomena, with low errors. However, for engineering purposes, the definition of the runup and, consequently, of potential flooded areas on an embayed beach, by employing empirical formulations based on equivalent wave height provide solutions that correspond to a safe-side attitude.

References

Antuono, M., Soldini, L., Brocchini, M., 2012. On the role of the chezy frictional term near the shoreline. Theoretical and Computational Fluid Dynamics 26, 105–116.

Atkinson, A.L., Power, H.E., Moura, T., Hammond, T., Callaghan, D.P., Baldock, T.E., 2017. Assessment of runup predictions by empirical models on non-truncated beaches on the south-east australian coast. Coastal Engineering 119, 15 – 31.

Battjes, J., 1974. Surf Similarity, in: Coastal Engineering 1974, American Society of Civil Engineers, New York, NY. pp. 466–480.

Benson, M.A., Dalrymple, T., 1967. General field and office procedures for indirect discharge measurements. Technical Report. US Govt. Print. Off.,.

Birkemeier, W.A., 1985. Field data on seaward limit of profile change. Journal of Waterway, Port, Coastal, and Ocean Engineering 111, 598–602.

Blenkinsopp, C., Matias, A., Howe, D., Castelle, B., Marieu, V., Turner, I., 2016. Wave runup and overwash on a prototype-scale sand barrier. Coastal Engineering 113, 88 – 103. Barrier Dynamics Experiment II: sediment processes across a large-scale sand barrier.

Booij, N., Holthuijsen, L.H., Ris, R.C., 1996. The" SWAN" wave model for shallow water. Coastal Engineering Proceedings 1.

Bouvier, C., Balouin, Y., Castelle, B., 2017. Video monitoring of sandbar-shoreline response to an offshore submerged structure at a microtidal beach. Geomorphology 295, 297 – 305.

Brocchini, M., Baldock, T.E., 2008. Recent advances in modeling swash zone dynamics: Influence of surf-swash interaction on nearshore hydrodynamics and morphodynamics. Reviews of Geophysics 46. https://agupubs.onlinelibrary.wiley.com/doi/pdf/10.1029/2006RG000215.

Bruno, M., Molfetta, M., Petrillo, A., 2014. The influence of interannual variability of mean sea level in the adriatic sea on extreme values. Journal of Coastal Research 70, 241–246.

Bruno, M.F., Molfetta, M.G., Pratola, L., Mossa, M., Nutricato, R., Morea, A., Nitti, D.O., Chiaradia, M.T., 2019. A combined approach of field data and earth observation for coastal risk assessment. Sensors 19, 1399.

Bruun, P., 1954. Coast erosion and the development of beach profiles. volume 44. US Beach Erosion Board.

Celli, D., Pasquali, D., De Girolamo, P., Di Risio, M., 2018. Effects of submerged berms on the stability of conventional rubble mound breakwaters. Coastal Engineering 136, 16–25.

Conde-Frias, M., Otero, L., Restrepo, J.C., Ortiz, J.C., Ruiz, J., Osorio, A.F., 2017. Swash oscillations in a microtidal dissipative beach. Journal of Coastal Research 33, 1408–1422.

De Roo, S., Suzuki, T., Kolokythos, G., Zhao, G., Verwaest, T., 2015. Numerical modelling of 2D wave transformation processes from nearshore to a shallow foreshore: comparison between the Mike21, swash and XBeach models, in: 36th IAHR World Congress, pp. 1–6.

Douglass, S.L., 1992. Estimating extreme values of run-up on beaches. Journal of Waterway, Port, Coastal, and Ocean Engineering 118, 220–224.

Elfrink, B., Baldock, T., 2002. Hydrodynamics and sediment transport in the swash zone: a review and perspectives. Coastal Engineering 45, 149–167.

Fonstad, M.A., Dietrich, J.T., Courville, B.C., Jensen, J.L., Carbonneau, P.E., 2013. Topographic structure from motion: a new development in photogrammetric measurement. Earth Surface Processes and Landforms 38, 421–430.

GEBCO, 2008. The GEBCO 08 Grid, ver. 20091120. General Bathymetric Chart of the Oceans .

Geosystems, L., 2001. Leica geosystems. System 500.

Gonçalves, J.A., Henriques, R., 2015. UAV photogrammetry for topographic monitoring of coastal areas. ISPRS Journal of Photogrammetry and Remote Sensing 104, 101–111.

Guimarães, P.V., Farina, L., Toldo, E., Diaz-Hernandez, G., Akhmatskaya, E., 2015. Numerical simulation of extreme wave runup during storm events in Tramandaí Beach, Rio Grande do Sul, Brazil. Coastal Engineering 95, 171–180.

Harwin, S., Lucieer, A., 2012. Assessing the accuracy of georeferenced point clouds produced via multi-view stereopsis from unmanned aerial vehicle (UAV) imagery. Remote Sensing 4, 1573–1599.

Henderson, S.M., Guza, R., Elgar, S., Herbers, T., Bowen, A., 2006. Nonlinear generation and loss of infragravity wave energy. Journal of Geophysical Research: Oceans 111.

Herbers, T.H.C., Elgar, S., Guza, R.T., 1994. Infragravity-frequency (0.005–0.05 hz) motions on the shelf. part i: Forced waves. Journal of Physical Oceanography 24, 917–927. https://doi.org/10.1175/1520-0485(1994)024<0917:IFHMOT>2.0.CO;2.

Holland, K., Puleo, J., 2001. Variable swash motions associated with foreshore profile change. Journal of Geophysical Research: Oceans 106, 4613–4623.

Holman, R.A., 1986. Extreme value statistics for wave run-up on a natural beach. Coastal Engineering 9, 527–544.

Holman, R.A., Stanley, J., 2007. The history and technical capabilities of Argus. Coastal Engineering 54, 477–491.

Hunt, I.A., 1959. Design of sea-walls and breakwaters. Transactions of the American Society of Civil Engineers 126, 542–570.

Lee, J.M., Park, J.Y., Choi, J.Y., 2013. Evaluation of sub-aerial topographic surveying techniques using total station and rtk-gps for applications in macrotidal sand beach environment. Journal of Coastal Research 65, 535–540.

Lerma, A.N., Pedreros, R., Robinet, A., Sénéchal, N., 2017. Simulating wave setup and runup during storm conditions on a complex barred beach. Coastal Engineering 123, 29–41.

Long, N., Millescamps, B., Guillot, B., Pouget, F., Bertin, X., 2016. Monitoring the Topography of a Dynamic Tidal Inlet Using UAV Imagery. Remote Sensing 8, 387.

Mancini, F., Dubbini, M., Gattelli, M., Stecchi, F., Fabbri, S., Gabbianelli, G., 2013. Using Unmanned Aerial Vehicles (UAV) for high-resolution reconstruction of topography: The structure from motion approach on coastal environments. Remote Sensing 5, 6880–6898.

Mase, H., 1989. Random wave runup height on gentle slope. Journal of Waterway, Port, Coastal, and Ocean Engineering 115, 649–661.

Mather, A.A., Stretch, D., Garland, G., 2011. WAVE RUN UP ON NATURAL BEACHES. Coastal Engineering Proceedings 1, 45.

Mayer, R.H., Kriebel, D.L., 1994. Wave runup on composite-slope and concave beaches. Coastal Engineering Proceedings 1.

39

Van der Meer, J.W., Stam, C.J.M., 1992. Wave runup on smooth and rock slopes of coastal structures. Journal of Waterway, Port, Coastal, and Ocean Engineering 118, 534–550.

Mentaschi, L., Besio, G., Cassola, F., Mazzino, A., 2015. Performance evaluation of Wavewatch III in the Mediterranean Sea. Ocean Modelling 90, 82–94.

Nielsen, P., 2009. Coastal and estuarine processes. volume 29. World Scientific Publishing Company.

Nielsen, P., Hanslow, D.J., 1991. Wave runup distributions on natural beaches. Journal of Coastal Research , 1139–1152.

Otsu, N., 1979. A threshold selection method from Gray-level. IEEE Transactions on Systems, Man, and Cybernetics SMC-9, 62–66.

Petrillo, F., 2014. SUPPORTO SCIENTIFICO PER LA REDAZIONE DEL PIANO COMUNALE DELLE COSTE DEL COMUNE DI PORTO CESAREO (LE). Technical Report. POLITECNICO DI BARI. Bari.

Poate, T.G., McCall, R.T., Masselink, G., 2016. A new parameterisation for runup on gravel beaches. Coastal Engineering 117, 176 – 190.

Reis, A.H., Gama, C., 2010. Sand size versus beachface slope – An explanation based on the Constructal Law. Geomorphology 114, 276–283.

Rijnsdorp, D.P., Ruessink, G., Zijlema, M., 2015. Infragravity-wave dynamics in a barred coastal region, a numerical study. Journal of Geophysical Research: Oceans 120, 4068–4089.

Rijnsdorp, D.P., Smit, P.B., Zijlema, M., 2014. Non-hydrostatic modelling of infragravity waves under laboratory conditions. Coastal Engineering 85, 30–42.

Ruggiero, P., Komar, P.D., McDougal, W.G., Marra, J.J., Beach, R.A., 2001. Wave runup, extreme water levels and the erosion of properties backing beaches. Journal of Coastal Research 17.

40

Salmon, S.A., Bryan, K.R., Coco, G., 2007. The use of video systems to measure run-up on beaches. Journal of Coastal Research 50, 211–215.

Sancho, A., Guillén, J., Simarro, G., Medina, R., Cánovas, V., 2012. Beach inundation prediction during storms using different wave heights as inputs. Coastal Engineering Proceedings 1, 32.

Saponieri, A., Damiani, L., 2015. Numerical analysis of infiltration in a drained beach. International Journal of Sustainable Development and Planning 10, 467–486.

Smit, P., Janssen, T., Holthuijsen, L., Smith, J., 2014. Non-hydrostatic modeling of surf zone wave dynamics. Coastal Engineering 83, 36–48.

Soldini, L., Antuono, M., Brocchini, M., 2012. Numerical modeling of the influence of the beach profile on wave run-up. Journal of Waterway, Port, Coastal, and Ocean Engineering 139, 61–71.

Stockdon, H.F., Holman, R.A., Howd, P.A., Sallenger Jr, A.H., 2006. Empirical parameterization of setup, swash, and runup. Coastal Engineering 53, 573–588.

Stockdon, H.F., Thompson, D.M., Plant, N.G., Long, J.W., 2014. Evaluation of wave runup predictions from numerical and parametric models. Coastal Engineering 92, 1–11.

Suzuki, T., Verwaest, T., Hassan, W., Veale, W., Reyns, J., Trouw, K., Troch, P., Zijlema, M., 2011. The applicability of swash model for wave transformation and wave overtopping: a case study for the flemish coast, in: Proc. 5th Int. Conf. Advanced Computational Methods Engineering (ACOMEN 2011), Liège, Belgium, pp. 14–17.

Svendsen, I.A., 2006. Introduction to nearshore hydrodynamics. volume 24. World Scientific.

Thévenaz, P., Sage, D., Unser, M., 2012. Bi-exponential edge-preserving smoother. IEEE Transactions on Image Processing 21, 3924–3936.

Thorndike Saville, J., 1957. Wave run-up on composite slopes. Coastal Engineering Proceedings 1, 41.

Tsimplis, M., Calafat, F.M., Marcos, M., Jordá, G., Gomis, D., Fenoglio-Marc, L., Struglia, M., Josey, S.A., Chambers, D., 2013. The effect of the nao on sea level and on mass changes in the mediterranean sea. Journal of Geophysical Research: Oceans 118, 944–952.

Tuan, T.Q., Oumeraci, H., 2010. A numerical model of wave overtopping on seadikes. Coastal Engineering 57, 757–772.

Turner, I.L., Harley, M.D., Drummond, C.D., 2016. Uavs for coastal surveying. Coastal Engineering 114, 19 – 24.

Valentini, N., Damiani, L., Molfetta, M.G., Saponieri, A., 2017a. New coastal video-monitoring system achievement and development. Coastal Engineering Proceedings 1, 11.

Valentini, N., Saponieri, A., Damiani, L., 2017b. A new video monitoring system in support of coastal zone management at apulia region, italy. Ocean & Coastal Management 142, 122–135.

Valentini, N., Saponieri, A., Molfetta, M.G., Damiani, L., 2017c. New algorithms for shoreline monitoring from coastal video systems. Earth Science Informatics 10, 495–506.

Vousdoukas, M., Kirupakaramoorthy, T., Oumeraci, H., De La Torre, M., Wübbold, F., Wagner, B., Schimmels, S., 2014. The role of combined laser scanning and video techniques in monitoring wave-by-wave swash zone processes. Coastal Engineering 83, 150–165.

Vousdoukas, M.I., Velegrakis, A.F., Dimou, K., Zervakis, V., Conley, D.C., 2009. Wave run-up observations in microtidal, sediment-starved pocket beaches of the Eastern Mediterranean. Journal of Marine Systems 78, S37–S47.

Vousdoukas, M.I., Wziatek, D., Almeida, L.P., 2012. Coastal vulnerability assessment based on video wave run-up observations at a mesotidal, steep-sloped beach. Ocean Dynamics 62, 123–137.

Westoby, M., Brasington, J., Glasser, N., Hambrey, M., Reynolds, J., 2012. Structure-from-motion photogrammetry: A low-cost, effective tool for geoscience applications. Geomorphology 179, 300–314.

Zijlema, M., Stelling, G., 2008. Efficient computation of surf zone waves using the nonlinear shallow water equations with non-hydrostatic pressure. Coastal Engineering 55, 780–790.

Zijlema, M., Stelling, G., Smit, P., 2011. SWASH: An operational public domain code for simulating wave fields and rapidly varied flows in coastal waters. Coastal Engineering 58, 992–1012.